Interrogating the Lewis Acidity of Metal Sites in Beta Zeolites with ^{15}N Pyridine Adsorption Coupled with MAS NMR Spectroscopy

Citation: Gunther, William R., Vladimir K. Michaelis, Robert G. Griffin, and Yuriy Román-Leshkov. "Interrogating the Lewis Acidity of Metal Sites in Beta Zeolites with ^{15}N Pyridine Adsorption Coupled with MAS NMR Spectroscopy." The Journal of Physical Chemistry C 120, 50 (December 2016): 28533–28544 © 2016 American Chemical Society

As Published: http://dx.doi.org/10.1021/ACS.JPCC.6B07811

Publisher: American Chemical Society (ACS)

Persistent URL: http://hdl.handle.net/1721.1/113314

Version: Author's final manuscript: final author's manuscript post peer review, without publisher's formatting or copy editing

Published in final edited form as:

J Phys Chem C Nanomater Interfaces. 2016 December 22; 120(50): 28533–28544. doi:10.1021/acs.jpcc.6b07811.

Interrogating the Lewis Acidity of Metal Sites in Beta Zeolites with ^{15}N Pyridine Adsorption Coupled with MAS NMR Spectroscopy

William R. Gunther[†,§,‖], **Vladimir K. Michaelis**[‡,§,‖], **Robert G. Griffin**[‡], and **Yuriy Román-Leshkov**[*,†]

[†]Department of Chemical Engineering, Massachusetts Institute of Technology, Cambridge, Massachusetts 02139, United States

[‡]Department of Chemistry and Francis Bitter Magnet Laboratory, Massachusetts Institute of Technology, Cambridge, Massachusetts 02139, United States

Abstract

The Lewis acidity of isolated framework metal sites in Beta zeolites was characterized with ^{15}N isotopically labeled pyridine adsorption coupled with magic-angle spinning nuclear magnetic resonance (MAS NMR) spectroscopy. The ^{15}N chemical shift of adsorbed pyridine was found to scale with the acid character of both Lewis (Ti, Hf, Zr, Nb, Ta, and Sn) and Brønsted (B, Ga, and Al) acidic heteroatoms. The ^{15}N chemical shift showed a linear correlation with Mulliken electronegativity of the metal center in the order Ti < Hf < Zr < Nb < Ta < Sn < H^+. Theoretical calculations using density functional theory (DFT) showed a strong correlation between experimental ^{15}N chemical shift and the calculated metal–nitrogen bond dissociation energy, and revealed the importance of active site reorganization when determining adsorption strength. The relationships found between ^{15}N pyridine chemical shift and intrinsic chemical descriptors of metal framework sites complement adsorption equilibrium data and provide a robust method to characterize, and ultimately optimize, metal-reactant binding and activation for Lewis acid zeolites. Direct ^{15}N MAS NMR detection protocols applied to the Lewis acid–base adducts allowed the differentiation and quantification of framework metal sites in the presence of extraframework oxides, including highly quadrupolar nuclei that are not amenable for quantification with conventional NMR methods.

Graphical abstract

[*]Corresponding Author: yroman@mit.edu. Tel: +1-617-253-7090.
[§]Present Address: (V.K.M.) Department of Chemistry, University of Alberta, Edmonton, Alberta, Canada T6G 2G2. (W.R.G.) ExxonMobil Research and Engineering Company, Annandale, New Jersey 08801.
[‖]Author Contributions: W.R.G. and V.K.M. contributed equally to this work.

Supporting Information: The Supporting Information is available free of charge on the ACS Publications website at DOI: 10.1021/acs.jpcc.6b07811. Methods for quantum chemical calculations, NMR parameters for various Lewis acid metals, data in infrared spectroscopy frequency for probe molecules, powder XRD patterns, elemental analysis data, surface area measurements, diffuse reflectance UV spectra, ^{15}N NMR chemical shift data and calculated parameters, structures of active site models (PDF)

Notes: The authors declare no competing financial interest.

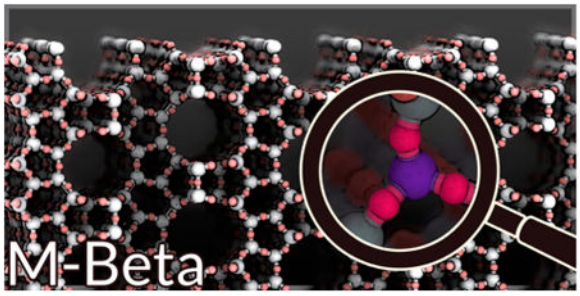

Introduction

Pure-silica zeolites containing framework metal centers with open coordination sites have emerged as highly active, water tolerant solid Lewis acids.[1–4] For example, framework metal centers, such as Ti, Hf, Zr, Nb, Ta, and Sn, have shown remarkable activity for the inter- and intramolecular Meerwein–Ponndorf–Verley (MPV) reduction of aldehydes and ketones,[5–7] the etherification of alcohols,[6,8,9] the Baeyer–Villiger oxidation of ketones to lactones,[10–12] the isomerization/epimerization of carbohydrates,[13–17] C–C coupling,[18–24] and hydrogen transfer reactions of high relevance to biomass conversion.[25–28] The nature of the metal center and the degree of framework incorporation drastically influence reactivity.[29] For example, Davis and co-workers showed that octahedral extraframework SnO_2 and pseudotetrahedral framework Sn sites can catalyze the same reaction through completely different reaction pathways.[30]

Distinguishing framework and extraframework sites within the confines of a zeolite pore is critical for assessing catalyst performance. Though reactivity studies provide the most direct measure of framework incorporation, catalysts often have a complex mixture of sites leading to an apparent overall activity. For example, in the isomerization of glucose to fructose with Sn-Beta, various authors have attributed the observed decrease in turnover frequency with increasing metal loading to the resence of framework Sn sites with different activities or the formation of condensed SnO_x species.[31,32]

Spectroscopic methods provide additional insight into the nature of active sites and have been used to obtain the site densities needed to calculate turnover frequencies. However, many of these methods are difficult to implement reliably or routinely.[6] For instance, diffuse reflectance ultraviolet spectroscopy (DRUV),[30,31,33] X-ray diffraction,[30,34] ^{119}Sn Mössbauer spectroscopy,[31] X-ray photoelectron spectroscopy (XPS),[33] and Raman spectroscopy[31,33] provide only qualitative or semi-quantitative measurements. Synchrotron-based techniques are powerful but difficult to implement on a routine basis.[34] Magic-angle spinning nuclear magnetic resonance (MAS NMR) spectroscopy can quantify the ratio of extraframework to framework metal sites but is limited to NMR-active nuclei. For instance, analysis of tin in Sn-Beta is accessible with NMR but requires expensive ^{119}Sn isotopic labeling.[6,16] Roman-Leshkov et al. and Hermans et al. have recently shown that hyperpolarization techniques based on dynamic nuclear polarization (DNP) MAS NMR can be implemented to characterize nonenriched Sn-Beta samples, but specialized NMR equipment is required.[31,35] Recently, Ivanova et al. showed that other methods could be used to obtain enhanced signals

with unlabeled samples.[36] Other metals of interest, including Ti, Zr, and Hf, suffer from extreme challenges in NMR sensitivity that stem from low natural abundance, large quadrupolar moment, and/or low gyromagnetic ratios (as shown in Table S1).[37]

The adsorption of probe molecules has been an effective technique to interrogate acid sites in zeolites. Infrared (IR) spectroscopy using pyridine to titrate solid acid sites has been utilized to distinguish Lewis and Brønsted acid sites and provide quantitation with molar extinction coefficients.[38] IR spectra of pyridine adsorption on zeolites has been used to determine acid strength of several heteroatoms based on differences in vibrational frequencies.[33] The frequencies for pyridine adsorbed on different Lewis acid sites (i.e., Ti, Zr, Nb, Ta, Sn, Ga, and Al-Beta) appears in a very narrow range from 1445 to 1454 cm^{-1} as shown in Table S2.[33,39–42] Gorte et al. showed that careful dosing of acetonitrile onto a dehydrated Sn-Beta sample gives rise to vibrational signatures of the resulting adducts that differentiate framework from extraframework sites with adequate resolution.[43] Recently, Gounder et al. determined molar extinction coefficients for IR bands of pyridine adsorbed to Lewis acidic Sn sites and of acetonitrile adsorbed to open and closed Sn sites.[44] Ivanova et al. used CO to characterize both types of sites. As shown in Table S3, limited data exists on the full range of Lewis acidic metals. Corma et al. performed a number of cyclohexanone adsorption experiments that cover a wider range (shown in Table S4), but the resonance widths at half-maximum of ~25 cm^{-1} do not provide a high degree of resolution. We note that IR has limitations when analyzing samples in the presence of water or other solvents due to unwanted adsorption frequencies that can interfere with quantitative analysis.

The magnetic shielding observed via NMR spectroscopy is highly sensitive to the local electronic environment about the observed nucleus. As such, changes in the chemical shift for a particular acid–base pair can be used to assess the Lewis acid character, to understand bond activation at a specific site without bulk effects due to nonspecific adsorption, and to infer binding strengths both under hydrated and dehydrated environments.[45–48] NMR has been used to characterize acidity of Lewis acid catalysts, for instance, by studying the interaction of trimethylphosphine (TMP), trimethylphosphine oxide (TMPO), and acetone with the active sites.[49] Similarly, ^{15}N MAS NMR of adsorbed pyridine has been used to distinguish multiple acid sites on γ-alumina with high resolution. Although pyridine ^{15}N MAS NMR has been used to probe the acidity of certain zeolites, the full range of Lewis acid metal-substituted Lewis acid zeolites has not been investigated with this method.[50–53]

Here, we assess the acid character of Beta zeolites with Lewis (Ti, Hf, Zr, Nb, Ta, and Sn) and Brønsted (B, Ga, and Al) acid centers by investigating the adsorption of pyridine with ^{15}N MAS NMR spectroscopy. We rationalize that the interaction of pyridine with the metal site leads to a change in chemical shift of the ^{15}N nucleus that can be correlated to fundamental measures of Lewis acidity, such as bond dissociation energies and Mulliken electronegativities. We show that the method is broadly applicable to investigate metal centers in zeolites under hydrated and dehydrated conditions. Using direct detection MAS NMR, we show that quantitative measurements can be performed on the pyridine-metal adducts, thereby yielding the ability to differentiate and quantify the number of framework metal centers, including NMR-inactive nuclei such as Zr and Hf.

Experimental Section

Catalyst Synthesis

Beta zeolites were synthesized based on the procedure reported by Corma et al.[54] using the following precursors: hafnium(IV) chloride, zirconium(IV) oxychloride octahydrate, tin(II) chloride dihydrate, titanium-(IV) isopropoxide, tantalum(V) ethoxide, and niobium(V) ethoxide. Tin(II), which oxidizes to tin(IV) in water, was used in place of $SnCl_4{\cdot}5H_2O$ and resulted in Sn-Beta consistently free of extraframework SnO_2.[55] Briefly, Hf-Beta was synthesized as follows: aqueous tetraethylammonium hydroxide [27.16 g; Sigma–Aldrich, 35 wt % (TEAOH)] and tetraethylorthosilicate (23.97 g; Sigma–Aldrich, 99 wt %) were added to a Teflon [polytetrafluoroethylene (PTFE)] dish, which was magnetically stirred at 250 rpm and room temperature for 90 min. Additional deionized water (15 mL) was added, and the dish was cooled in an ice bath. Then hafnium(IV) chloride (0.38 g; Sigma–Aldrich, 98 wt %) dissolved in ethanol (2 mL) was added dropwise while stirring. The solution was left uncovered on the stir plate for 10 h to reach a total mass of 33.15 g after evaporation of ethanol and some of the water. Next, aqueous hydrofluoric acid (HF, 2.62 g; Sigma–Aldrich, 48 wt %) was added dropwise using a plastic syringe, and the mixture was homogenized using a PTFE spatula, resulting in a thick gel. Si-Beta (0.36 g) was seeded into the mixture. The preparation of Si-Beta is analogous to Sn-Beta but without seeding or metal addition. The weight of the resulting sol–gel was evaporated under light heating to 33.96 g over ca. 2 h, resulting in a final molar composition of 1 SiO_2/0.01 $HfCl_4$/0.56 TEAOH/0.56 HF/7.5 H_2O. The thick paste was transferred to a PTFE-lined stainless steel autoclave (45 mL) and heated to 413 K for 20 days under static conditions. Mixing the contents weekly can accelerate crystallization. The solids were recovered by filtration, washed with ultrapure deionized H_2O, and dried at 373 K. The zeolites were calcined under flowing dry air by heating to 853 K with a 1 K min^{-1} ramp (with 1 h isothermal steps at 423 and 623 K) and kept at that temperature for 10 h. After calcination, the overall inorganic oxide yield was 80–90%.

Sn-MCM-41 and Sn-MFI were synthesized according to previously published protocols using alkaline media.[56,57] SnO_2/Si-Beta was prepared by incipient wetness impregnation of Si-Beta with an aqueous tin(IV) chloride solution, followed by drying at 383 K and calcination in air flow at 533 K. Mixed framework/extraframework ^{119}Sn-Beta was made by calcination of the as-prepared material in a box furnace at 1173 K for 10 h with a 1 K min^{-1} ramp and 1 h stops at 423 and 623 K flowing 100 mL/min of dry air. We note that analogous experiments showed negligible extraframework SnO_2 formation up to a temperature of 1073 K, while temperatures above 1273 K led to pore collapse.

Catalyst Characterization

Inductively coupled plasma atomic emission spectroscopy (ICP-AES) was recorded on an Optima 2000 DV spectrometer (PerkinElmer Inc.). Samples were dissolved in a few drops of 35% HF before dilution into 2.5% HNO_3. Powder X-ray diffraction (PXRD) patterns were collected using a Bruker D8 diffractometer using a Cu Kα radiation source between 5 and 45° 2θ, in 0.02° steps with a step time of 30 s. Ultraviolet/visible (UV/vis) analysis was performed using a Varian Cary 5000 UV/vis near-infrared spectrometer equipped with a

Praying Mantis diffuse reflectance accessory. The spectra were collected at 190–450 nm and referenced to $BaSO_4$. N_2 adsorption–desorption isotherms were measured on a Quantachrome Autosorb iQ apparatus at liquid-nitrogen temperature (77 K). All samples were degassed under vacuum prior to use (623 K, 12 h). Micropore volumes were analyzed using the t-plot method.

Pyridine Adsorption

Sample preparation consisted of weighing 100 mg of the catalyst, sealing in a 5 mL microwave vial and connecting to a Schlenk line. The air within the sample was purged out by alternating three times between vacuum and Ar, followed by heating the sample to 423 K for 2 h under dynamic vacuum. We note that these conditions have been shown to be sufficient to dehydrate defect-free Lewis acid zeolites synthesized in fluoride media. Samples were predried before pyridine adsorption to promote uniformity among the sites and prevent competitive adsorption. The sample vial was refilled with Ar and removed from the Schlenk line. Next, ^{15}N-labeled pyridine adsorption was performed by flowing pyridine saturated Ar over the sample at 423 K. Specifically, the vial containing the dried zeolite sample was connected with a cannula to another purged and septum-sealed vial containing ^{15}N pyridine under Ar flow (~30 mL/min). An open needle was then inserted into the vial containing the zeolite to avoid pressure build-up. For weakly binding oxide samples, such as SnO_2–Beta, ZrO_2–Beta, and Si-Beta, the adsorption temperature was reduced from 423 to 373 K. After 30 min, the sample vial was isolated, reconnected to the Schlenk line, and placed under vacuum for 1 h at the corresponding adsorption temperature to remove physisorbed pyridine. Afterward, the sample was transferred into a glovebox where it was opened and packed into an O-ring sealed ZrO_2 NMR rotor. For experiments probing hydrated sites, the zeolite sample was exposed to ambient moisture after dosing with pyridine.

For quantitative runs, 10 mg of dry 98% ^{15}N-labeled glycine (Cambridge Isotope Laboratories, Andover, MA) was used as an internal standard by mixing together with the pyridine-dosed catalyst using a glass stir rod before packing into a rotor. For all pyridine quantitation experiments, zeolites were calcined under dry air immediately before pyridine dosing.

Nuclear Magnetic Resonance

MAS NMR experiments were performed on home-built spectrometers (courtesy of D.J. Ruben, Francis Bitter Magnet Laboratory, Massachusetts Institute of Technology) operating at 360 and 500 MHz (^1H Larmor frequency). The 360 MHz NMR spectrometer was equipped with either a double resonance home-built (FBMLMIT) or a triple resonance Varian-Chemagnetics probe (Palo Alto, CA), which were doubly tuned to $^{119}Sn/^1H$. The 500 MHz NMR spectrometer was equipped with a triple resonance Varian-Chemagnetics probe (Palo Alto, CA) doubly tuned to $^{15}N/^1H$. Powdered samples were packed into either 3.2 mm (26 μL fill volume) or 4 mm (80 μL fill volume) outer diameter ZrO_2 rotors equipped with Vespel drive- and top-caps. Top-caps were equipped with rubber O-ring seals to inhibit water contamination of the sample (Revolution NMR, Fort Collins, CO). Dry samples were

prepared by heating to 423 K under a 10 Pa vacuum and packing the NMR rotor in an Ar-filled glovebox.

^{15}N cross-polarization (CP)[58] MAS NMR spectra were acquired with a spinning frequency set to 9 kHz ($\omega_r/2\pi$) and regulated with a Bruker (Billerica, MA) MAS controller. The recycle delay was set to 1.5 s, 64k coadded transients were acquired, and the temperature was maintained at 290 K. The spin-lock on ^{15}N during CP was optimized to match the Hartmann–Hahn condition[59] under MAS with $\gamma B_1/2\pi$ = 50 kHz on protons during a contact time of 2.0 ms, which was maintained constant for all samples. Proton pulses and two pulse phase modulation (TPPM) decoupling[60] were optimized for $\gamma B_1/2\pi$ = 83 kHz. All spectra were referenced externally to liquid ammonia (0 ppm of NH_3). CP MAS NMR revealed the bound Brønsted sites and selectively probed bound pyridine molecules. ^{15}N chemical shielding anisotropy experiments[61] were acquired using CP MAS NMR at a spinning frequency of 5 kHz (Supporting Information).

For quantitative purposes, ^{15}N MAS NMR analyses used direct detection (Bloch) and spin–lattice relaxation times (T_1) were measured using either an inversion recovery or saturation recovery experiment. Typical T_1's were on the order of 200 to 800 ms for ^{15}N, and recycle delays were chosen to be 5 times T_1 (or greater) for all NMR experiments. All spectra were acquired using a 9 kHz spinning frequency and between 16384 and 32764 coadded transients. Spectra were processed using 125 Hz of an exponential apodization function. Spectra fitting of the pyridine and glycine resonances were performed using a single Lorentzian and the baseline with one sine function using least-squares. All quantitative data were carefully fitted to account for the spinning sideband intensity of the larger CSA of bound pyridine (span, Ω = 370 ppm, skew, κ = 0.8) relative to the internal ^{15}N glycine (Ω < 15 ppm, κ = 0.05) standard.

^{119}Sn MAS NMR spectra were acquired by performing a Hahn-echo (^{119}Sn, $\gamma B_1/2\pi$: = 50 kHz) with recycle delays between 10 and 40 s, between 8192 and 35850 coadded transients, and a spinning frequency of 8 kHz. Typical T_1's were on the order of 2 to 8 s for ^{119}Sn and recycle delays were chosen to be 5 times T_1 of the slowest relaxing site. ^{119}Sn spectra were referenced externally using a secondary reference solid, SnO_2 (−604.3 ppm, relative to tetramethyltin, 0 ppm).

Quantum Chemical Calculations

Detailed methods can be found in the Supporting Information. Simulations were run on a Unix cluster implementing Gaussian G09, revision B.01.[62] A 17 tetrahedral model (17 T) of the Beta zeolite T2 site was created from the International Zeolite Association (IZA) crystallographic structure, and the outer atoms were frozen with hydrogen atoms pointing in the direction of missing oxygen atoms for cluster termination. Hybrid density functional theory (DFT) geometry optimizations and energies were performed at the B3LYP/Def2-TZVPD level of theory,[63–65] and counterpoise corrections were applied to remove basis set superposition error. All of the metal atoms except Ti used an effective core potential (ECP). The reported energy values represent the electronic contribution to enthalpy and were not adjusted for the thermal correction since the vibrational frequencies of the zeolite cluster may be nonphysical. Additional data were gathered at B3LYP/Def2-TZVP and Def2-TZVPP

to demonstrate convergence. Detailed descriptions of the methods used appear in the Supporting Information.

Results and Discussion

The adsorption of ^{15}N-pyridine onto metal-substituted zeolites will form adducts that feature specific ^{15}N isotropic chemical shifts (δ_{iso}). The ^{15}N δ_{iso} of pyridine and pyridinium (protonated pyridine) are 317 and 211 ppm, respectively, yielding a 106 ppm chemical shift range that can be used to assess the acid character of specific pyridine-acid adducts.[66,67] Note that pyridine adsorption on an acid site causes a reduction in the span (Ω) of the ^{15}N CSA and the δ_t component, which lies in the plane of and tangential to the pyridine ring. This change appears as δ_{11} and δ_{22} in the chemical shift tensor for pyridine and pyridinium, respectively.[67] Consequently, after binding to an acid, the pyridine resonances will appear at lower frequency, which is opposite to the expected trend for the interaction between electron density-withdrawing sites and electron density-shielding nuclei (see Figure 1).

Figure 2 shows the ^{15}N δ_{iso} of pyridine adsorbed on a series of porous materials, including pure silica zeolites, metal-substituted and metal-impregnated zeolites, as well as mesoporous Sn-MCM-41. In the absence of framework metals, the defect-free Si-Beta showed no resonances associated with pyridine, while Si-Beta containing extraframework Sn and Zr oxides showed very weak Lewis acidity, with the appearance of a ^{15}N resonance near 318 ppm. Taken together, these control experiments show that in the absence of framework metal sites, pyridine does not interact with a defect-free zeolite framework and that extra-framework heteroatoms feature ^{15}N chemical shifts to higher frequency (increase in ppm) of the chemical shift scale that correspond to weakly (or physisorbed) bound pyridine molecules. Our findings also agree with other surface and mesoporous silica studies as summarized in Table 1.

The ^{15}N δ_{iso} of pyridine resolves the Brønsted acids in the expected order of acid strength as follows: silanols < B-Beta < Ga-Beta < Al-Beta. The resonance at 288 ppm for weakly acidic silanols defines a lower limit of Brønsted acid strength. The fluoride synthesized Al-Beta showed a chemical shift of 212 ppm that is consistent with a fully protonated pyridine molecule, thus defining the upper limit of Brønsted acid strength in this scale (see Figure 3).

In contrast to Brønsted acid sites, the interaction of pyridine with a Lewis acid site leads to a more diverse chemical shift range. This phenomenon can be rationalized from the Ramsey expression for NMR chemical shift by noting that the energy of the nitrogen sp^2 lone pair electron is located just below that of an antibonding π orbital associated with the pyridine ring.[73] Binding to a Lewis acid allows the nitrogen electron lone pair to enter a definite lower energy σ bond with each metal center, leading to larger transitions to the antibonding π orbital and, consequently, a smaller chemical shift component. The isotropic chemical shift is the average of the chemical shift components, and a reduction in the δ_t chemical shift component moves the resonance to lower frequency (i.e., closer to pyridinium). Interestingly, the radial (δ_{22} in pyridine and δ_{11} in pyridinium) and perpendicular (δ_{33}) components of the chemical shift tensor are related exclusively to electronic transitions internal to the pyridine molecule. Since the lone pair is not involved in pyridine ring

resonance and the pyridine geometry does not change drastically upon binding to a Lewis acid site, these chemical shift components are not significantly perturbed upon adsorption. Taken together, these features provide a robust and highly sensitive probe for assessing Lewis acid character.

For our samples, the ^{15}N δ_{iso} of pyridine resolves the Lewis acid centers over a 20 ppm range, with the following order: Ti < Hf < Zr < Nb < Ta < Sn. Among the different Sn-containing structures, Sn-Beta shows the highest frequency Lewis acid character with a ^{15}N chemical shift of 260 ppm. Two overlapping ^{15}N pyridine resonances are observed for most materials, which we hypothesize correspond to the strong and weak sites in analogy with the two ^{119}Sn resonances observed in the ^{119}Sn NMR spectrum of dehydrated samples for tetrahedrally coordinated Sn atoms.[6,16] Sn-MFI and the mesoporous Sn-MCM-41 have similar Sn resonances centering at 262 ppm as well as a resonance near 285 ppm consistent with the presence of silanol groups (i.e., Si–OH---pyridine) in the framework.[70] In an earlier work, Van der Waal et al. mention that, as a hard Lewis acid, Ti prefers hard Lewis bases such as oxygen over pyridine (a Lewis base with intermediate hardness).[74] In the presence of silanol groups, the authors suggest that pyridine would preferentially deprotonate the Brønsted acidic silanol group rather than coordinating directly with the Lewis acid site. However, we observe that the δ_{iso} of ^{15}N pyridine adsorbed on Ti-Beta (281 ppm) is distinct from that on Si-Beta with defect sites (288 ppm), indicating that pyridine likely preferentially interacts with framework Ti sites. The δ_{iso} of ^{15}N pyridine adsorbed on framework Sn (ca. 263 ppm) is drastically different from that adsorbed on extraframework SnO_2 (319 ppm), and similarly, the δ_{iso} of ^{15}N pyridine adsorbed on framework Zr (275 ppm) differs from that adsorbed on extraframework ZrO_2 (318 ppm). Hf and Zr have similar resonances because Hf appears below Zr in the periodic table, and the elements have similar covalent atomic radii due to the lanthanide contraction (i.e., 1.50 vs 1.48 Å). Nb and Ta show intermediate ^{15}N δ_{iso} of 274 and 268 ppm, respectively. These metals are active in many reactions catalyzed by isolated framework Hf, Zr, and Sn sites and offer a higher charge to radius ratio. Sn- and Ta-containing samples also exhibited small resonances associated with strong Brønsted acidity near 210 ppm. For Ta, this effect may result from an inductive effect of the =O group similar to that observed in sulfated zirconia. These NMR trends are in agreement with prior work investigating probe molecule adsorption on zeolites with IR spectroscopy (vide supra).

In order to understand the catalytic behavior of Lewis acid sites in the presence of water, additional ^{15}N MAS NMR experiments were performed to study the substituted Beta zeolites under hydrated conditions. We anticipated that water would interact strongly with the metal site in the hydrophilic materials but more weakly in the hydrophobic materials, thereby influencing hydrogen bond networks near the active site.[75,76] For the fluoride-synthesized zeolites, the results of pyridine adsorption are indistinguishable for dehydrated and hydrated samples, thus showing that the ^{15}N chemical shift data generated under dehydrated conditions may be applicable to hydrophobic materials under hydrated conditions. Extended silanol nests in hydrophilic materials can stabilize hydrogen bond networks and promote the presence of an extended water network in the pores. This effect is manifested in the slight changes in isotropic chemical shift for the hydroxide-synthesized and mesoporous materials that feature defect sites and terminal hydroxyl groups. As shown

in Figure 2, a slight shift to lower frequency (decrease in ppm) in the leftmost ^{15}N resonance is observed for the Sn-MFI and Sn-MCM-41 samples, which is consistent with a displacement of pyridine from the weakest sites with water.[70]

Changes in the width of the isotropic chemical shift and chemical shift anisotropy provide further information on the modes of complexation between pyridine and the metal center, while numerical analysis of the spinning sideband pattern provides additional structural information.[77] The wide resonances observed for Ti-Beta correspond to a high degree of flexibility for the pyridine-Ti adduct geometry. The ability for ^{15}N-pyridine molecules to bind to various T-sites is thought to limit our ability to resolve ^{1}J(M, ^{15}N) (where M = ^{27}Al, $^{69/71}$Ga, ^{93}Nb, and ^{181}Ta) J-couplings. J-couplings between ^{15}N-pyridine and highly abundant NMR-active nuclei may contribute to the breadth of the ^{15}N isotropic chemical shift, as shown previously in pyridine-containing cobalt coordination complexes [^{15}N–^{59}Co (100% N.A.)].[71] Slow-spinning experiments to study the chemical shift anisotropy (CSA) are shown in Figure S6 and summarized in Table 1. Sn and Zr showed nearly identical patterns consistent with a similar orientation of the chemical shift tensor. Additionally, a hydrated Sn-Beta showed the rise of a disordered structure between 210 and 215 ppm, which we attribute to pyridinium interacting with the metal center or simply residing as a physisorbed species within the pores.

Assessing Lewis Acidity

Using the ^{15}N isotropic chemical shift to assess Lewis acidity enables us to establish correlations with fundamental measures of Lewis acidity. There have been many attempts to find a fundamental parameter that quantifies Lewis acidity, which has proven to be particularly difficult for solids. The simplest and most widely used measure is the binding strength of a basic molecule onto an acid site. The most fundamental description for this interaction is represented by Fukui functions that describe the electron density in a frontier orbital resulting from a small change in the total number of electrons. These functions can be used to determine the degree of electrophilicity of an active site. Pearson et al. showed that the Mulliken electronegativity (χ) and the hardness (η), analogous to the first- and second-derivatives of energy with respect to number of electrons, respectively, can be used to measure Lewis acidity with more accuracy.[78] Applying a finite difference approximation for the first derivative and three-point finite difference approximation for the second derivative leads to operational definitions in terms of ionization potential (I) and electron affinity (A) as follows:

$$\chi = -\mu = -\left(\frac{\partial E}{\partial N}\right)_{\nu} = \frac{1}{2}(I + A) \quad (1)$$

$$\eta = \frac{1}{2}\left(\frac{\partial^2 E}{\partial N^2}\right)_{\nu} = \frac{1}{2}(I - A) \quad (2)$$

where μ is electronic chemical potential, E is the energy, N is the number of electrons, and V is the potential. As such, the Mulliken electronegativity can be interpreted as a finite difference approximation of the electronic energy with respect to the number of electrons, which provides a measure of how strongly a Lewis acid site can polarize a reactant.

Hard–soft acid base theory (HSAB) uses chemical hardness to describe deviations from a pure electronegativity analysis. Indeed, such deviations exclude the possibility of establishing a universal scale for all Lewis acid–base interactions. The HSAB theory suggests that hard acids prefer to bind with hard bases and soft acids prefer to bind with soft bases. When the difference between the highest occupied molecular orbital (HOMO) of the donor and lowest unoccupied molecular orbital (LUMO) of acceptor is large, charge control involving electrostatic interactions is dominant, and hard–hard interactions are favored, while for smaller differences, frontier-orbitals at the outer edge of a molecule are dominant. In the numerical version of HSAB, represented in eq 3 below, the difference in electronegativity drives the electron transfer and the sum of the hardness parameters acts as a resistance leading to an overall charge transfer of ΔN where C refers to the Lewis acid and B to the base. HSAB however does not take into account the shapes and phases of the participating orbitals, says little about hard–soft complexes, and fails to explain variations in the strength of bonds.

$$\Delta N = \frac{\chi_{\mathrm{C}} - \chi_{\mathrm{B}}}{2(\eta_{\mathrm{C}} + \eta_{\mathrm{B}})} \quad (3)$$

Several different measures of Lewis acidity have been proposed, including LUMO energy, electronegativity, degree of electron transfer, and strength of interaction between the acid–base pair. Corma et al. proposed using the LUMO energy of a mixed oxide as a measure of Lewis acidity; however, the authors noted that this comparison only holds for Lewis acid sites of the same central atom, in the same valence state, and with the same coordination number.[79] LUMO energies are difficult to obtain experimentally but correlate linearly with electron affinity.[80] Similarly, the HOMO energies correlate with ionization potential, and the HOMO–LUMO gap is important to determine the extent of interaction between an acid base pair.

The values of the relevant parameters describing Lewis acid character for different metals are summarized in Table 2.

As shown in Figure 4, electron affinity and Mulliken electronegativity show a linear correlation with the experimentally determined ^{15}N isotropic chemical shift values (or averaged isotropic chemical shift from the resonances of strong and weak sites). Furthermore, using the proton electronegativity for Al-Beta-F shows that the linear trend extends over the entire chemical shift range spanned by Lewis and Brønsted acid sites. The observed ^{15}N pyridine trend is noteworthy because it captures the interaction of pyridine with metal centers featuring significantly different electronic states (Figure 3). We note that different coordination environments often lead to different chemical shifts, especially for polarizable metal atoms. Also, nitrogen is directly bound to the metal, and the reduction of

chemical shielding anisotropy not directly related to the metal's ability to function as a Lewis acid points to a more fundamental association. We posit that the linear correlation between the ^{15}N isotropic chemical shift and Mulliken electronegativity occurs because of the correspondence between the HOMO–LUMO energy gap and the ionization energy-electron affinity energy gap. The former appears in the Ramsey expression of chemical shift and the latter in the definition of Mulliken electronegativity. The similarity in the M–O–Si coordination environment facilitates establishing such correlation. The partial electron transfer (ΔN) calculated according to eq 3 does not alter the trend, suggesting that the hard–soft nature of the system does not significantly perturb the chemical shift.

Quantum Chemical Calculations

The strength of interaction between the acid–base pair is proportional to orbital overlap and inversely proportional to its HOMO–LUMO energy difference. Adsorption isotherms at multiple temperatures or calorimetry can provide experimental measures of pyridine binding strength; however, these techniques have technical challenges, and competing effects are difficult to separate. Evidently, covalent bonding in an acid–base pair is a function of many parameters other than the degree of electron transfer. Quantum chemical calculations are ideal to determine the metal–nitrogen bond dissociation energies and the energetics associated with active site reorganization.

Specifically, density functional theory (DFT) provides fundamental insight into the structure and bonding of the catalyst substrate complex such as bond distances and charge distributions in order to support the use of chemical shift as a proxy to evaluate Lewis acidity. DFT includes the effects of orbital overlap and provides a deeper understanding of HOMO–LUMO interactions. Determining the pyridine dissociation energy and geometric distortion energy of the metal site can address the possibility that reactant activation can differ from adsorption enthalpy due to geometric changes induced by the flexibility of the metal in the framework. Additionally, NMR calculations allow comparing calculated chemical shielding components with experimental data to validate the model and verify pyridine complexation on specific metal sites. Consistency between the two sets of data facilitates assignment of resonances and rule out the binding of multiple pyridine molecules on a single site.

To this end, we developed a 17 tetrahedral site model that incorporates both geometric constraints and local distortion of the crystal lattice. Specifically, the model fixes the outer atoms at specific crystallographic locations, but allows the inner five tetrahedral sites with their associated oxygen atoms to relax (see Figure S7). Heteroatom substitutions were confined to the T2 site of a Beta zeolite, in accordance with prior studies suggesting the preferential substitution of Sn into this site.[81] Nb and Ta exist in a +5 oxidation state and were modeled with a M=O functional group. We note that the present study did not model the preferential substitution of small B, Al, and Ga atoms, which may localize to other sites. Simulations starting with two pyridine molecules resulted in one of the two molecules moving away from the metal site; consequently, the cluster models included only a single pyridine molecule bound to a single metal center.

The model for Sn-Beta was extended by one shell of oxygen atoms (see Figure S7) in order to allow relaxation of both shells of Si atoms near the Sn center. For groups IV and V transition metals, the LUMO is the unfilled dz^2 orbital, which is less sensitive to the coordination geometry. In contrast, the LUMO of Sn is a linear combination of the 4 Sn–O σ^* orbitals, making bonding very sensitive to coordination geometry. Sn delocalizes electron density from an incoming base to its four adjacent framework oxygen atoms, lengthening and polarizing its bonds in the process and resulting in a distortion of the crystal lattice. Even without substrate binding, X-ray adsorption spectroscopy (XAS) data on Sn-Beta had previously shown distortion of the Beta lattice to at least two Si atoms away from the Sn site.[34]

Table 3 shows the results of the geometry optimization for several Lewis acid zeolites. There is a strong correlation between the dative covalent bond length and bond dissociation energy for all six substituted zeolites, which suggests that a 30 kJ/mol increase in adsorption energy brings the nitrogen 0.1 Å closer to the metal site. As shown in Figure 5, the metal-N bond dissociation energies show a strong correlation with experimental ^{15}N chemical shift values, indicating consistency between the two Lewis acidity scales. The good fit presumably results from error cancellation associated with adsorption energy as an energy difference. In Figure 5, Sn appears ca. 23% off the trend line, likely because of limited flexibility of the cluster model combined with not accounting for expansion of the zeolite unit cell. Hf also showed a ca. 16% offset from the trend line likely due to the presence of f-electrons with stronger σ bonding.[82]

Allowing the metal site to return to its most stable state without pyridine resulted in geometric distortion energies analogous to those reported by Bell et al.[75] The calculated geometric distortion energies also correlate with chemical shift. Relaxation of the metal site can recover a portion of the metal pyridine dissociation energy, and the sum of the dissociation and the geometric distortion energy provides an estimate of the adsorption energy. The trend resembles a plot for catalyst active site distortion energy versus heteroatom radii,[75] potentially due to the near linear trend of chemical shift with metal-N bond length. This trend may correlate to the atomic radii and polarizability discussed by Bell et al.[75] As an additional correlation illustrating Lewis acidity changes in metal-substituted zeolites, pyridine Mulliken charges are plotted in Figure S8 and show increasing charge transfer to the metal cluster with increasing Lewis acidity. Def2-TZVP and Def2-TZVPP calculations trend better than Def2-TZVPD likely resulting from the greater basis set balance without diffuse functions.

As shown in Figure S8, NMR calculations on the structures showed the expected correlation between calculated ^{15}N isotropic chemical shielding and experimental isotropic chemical shift, suggesting the model involving a single pyridine bound directly to the metal center adequately represents the system. The simulations also showed that stronger Lewis acids had smaller chemical shift anisotropies resulting from movements of the δ_{33} chemical shift component, which is consistent with the description of the pyridine system put forth at the beginning of the Results and Discussion section. Chemical shift anisotropy contains directionally dependent information, and the similar pattern suggests a similar complex structure, a requirement to function as an effective probe of Lewis acidity. The reduction of

the ^{15}N CSA observed here when compared to pyridine can be explained by the pyridine binding to a metal site within the Beta-zeolite[67,69,71] and a fast axially symmetric C_2 rotation of the pyridine ring as described by Shenderovich et al., further supported by our fast ^{15}N T_1 values[69] and poorer efficiency in the CP-based NMR experiments. We note that it is important to perform both direct and CP-based experiments in order to identify free pyridine when performing these studies.

The systems of interest have a number of computational challenges, including the presence of inorganic and organic groups, high valence heavy metal atoms with relativistic corrections, aromatic bonds within the pyridine, and diffuse lone pairs. These challenges are addressed in more detail in the Supporting Information. We note that the largest source of error is the finite cluster size. Owing to the computational complexity of modeling an entire zeolite pore, the model neglected the effects of nonspecific physisorption. Typically, physisorption resulting from van der Waals forces involves an enthalpy change as high as 40 kJ/mol. Corma et al. showed a 60 kJ/mol adsorption energy for toluene adsorption on fluoride synthesized Si-Beta.[83] Application of the dispersion-corrected ωB97X-D functional on the Sn 17T cluster model increased the binding energy by approximately 30 kJ/mol. These differences should not affect the trends between the different substituted Beta zeolites but would result in an offset when using small molecules such as pyridine and glycine to relate calculated and experimental values. A larger periodic model might better address expansion of the Beta unit cell and the potential for double Sn substitutions.

Quantifying Framework Sites

Direct detection methodologies using ^{15}N glycine as an internal standard were used to indirectly quantify the framework metal sites in ^{119}Sn-Beta and Zr-Beta zeolites. A linear correlation was observed between the amount of adsorbed pyridine and framework tin content (calculated from ^{119}Sn MAS NMR data and ICP analyses) for samples with Si/Sn molar ratios ranging from ca. 100 to 350 (see Figure 5). This correlation can be used as a calibration curve to determine framework content for any metal in a Beta zeolite. To demonstrate the applicability of the method to quantify framework atoms even in the presence of extraframework species, a pristine ^{119}Sn-Beta sample (Si/Sn = 115) was subjected to a heat treatment with the purpose of converting framework tin species into extraframework SnO_2 clusters. Heating the sample at 1173 K for 10 h in dry air converted 14% of the framework atoms into extraframework species (as determined by ^{119}Sn MAS NMR). Nitrogen adsorption data confirmed that the structure (i.e., crystallinity and micropore volume) of the zeolite structure remained intact after heat treatment (see Table S6). The ^{15}N pyridine MAS NMR quantification method effectively captured the change in framework content. Importantly, this method can be applied to quantify metal centers that cannot be easily analyzed directly with NMR. For example, as shown in Figure 6, the Zr content of various Zr-Beta samples was successfully quantified with this approach. We note that a recent infrared spectroscopy study suggested that pyridine can only access 62% of Sn sites in Sn-Beta, which contrasts the near quantitative adsorption values observed for our samples.[84] We hypothesize that the difference in dosing temperatures between both studies (423 vs 323 K) impacts the diffusion and adsorption events within the entirety of the zeolite crystal.[84]

Conclusion

A ^{15}N MAS NMR-based method is presented for assessing the strength and number of framework metal sites using pyridine as a probe molecule. MAS NMR analysis of the ^{15}N chemical shift of adsorbed pyridine on metal-substituted zeolites (e.g., Sn, Ti, Zr, Hf, Nb, Ta, B, Ga, and Al) shows linear correlations with several fundamental descriptors and is applicable to heteroatoms that are difficult to analyze with traditional methods. ^{15}N MAS NMR spectra of pyridine displayed good resolution for both Lewis and Brønsted acids and control experiments showed complete resolution of framework sites from inactive SnO_2. Spectra of these water tolerant solid acids were obtained under dehydrated and hydrated conditions, showing the role of water in hydrophilic materials. The ^{15}N chemical shift of pyridine resolved the identity of different heteroatoms in Beta zeolite, including framework sites in the presence of extraframework oxides. A linear correlation of ^{15}N chemical shift with Mulliken electronegativity was found which is consistent with the HSAB theory of Lewis acidity. DFT studies demonstrated the utility of adsorption energy as a measure of Lewis acidity and illustrated the importance of considering active site reorganization when computing adsorption equilibrium. The selective insight generated by this technique into activation of framework sites complements adsorption equilibrium data and facilitates rational catalyst selection to optimize reactant binding. Lewis acids are more diverse than Brønsted acids and this diversity offers the ability to develop highly selective processes. This method is general and can be easily implemented to compare the Lewis acid strength of samples with the same heteroatom but synthesized with different methodologies.[32,85–88] Recent kinetic results on the substituted Beta materials[89] suggest that higher solvent polarity results in tighter binding to the Lewis acid center and decreased flexibility in the transition state. Current efforts are focused on investigating the impact of condensed phases and solvents with different dielectric constants on binding properties.

Supplementary Material

Refer to Web version on PubMed Central for supplementary material.

Acknowledgments

The authors acknowledge financial support for this work from the U.S. Department of Energy, Office of Science, Office of Basic Energy Sciences, Chemical Sciences, Geosciences and Biosciences Division under Grant DE-SC0016214. We acknowledge the National Institutes of Health for funding support of the MIT-Harvard Center for Magnetic Resonance Facility at the Francis Bitter Magnet Laboratory (EB-002026). V.K.M. is grateful to the Natural Sciences and Engineering Research Council of Canada and Government of Canada for a Banting Postdoctoral Fellowship.

References

1. Corma A, Garcia H. Lewis Acids: From Conventional Homogeneous to Green Homogeneous and Heterogeneous Catalysis. Chem Rev. 2003; 103:4307–4366. [PubMed: 14611265]
2. Ennaert T, Van Aelst J, Dijkmans J, De Clercq R, Schutyser W, Dusselier M, Verboekend D, Sels BF. Potential and Challenges of Zeolite Chemistry in the Catalytic Conversion of Biomass. Chem Soc Rev. 2016; 45:584–611. [PubMed: 26691750]
3. Roman-Leshkov Y, Davis ME. Activation of Carbonyl-Containing Molecules with Solid Lewis Acids in Aqueous Media. ACS Catal. 2011; 1:1566–1580.

4. Moliner M. State of the Art of Lewis Acid-Containing Zeolites: Lessons from Fine Chemistry to New Biomass Transformation Processes. Dalton Trans. 2014; 43:4197–4208. [PubMed: 24142026]
5. Bui L, Luo H, Gunther WR, Román-Leshkov Y. Domino Reaction Catalyzed by Zeolites with Brønsted and Lewis Acid Sites for the Production of γ-Valerolactone from Furfural. Angew Chem, Int Ed. 2013; 52:8022–8025.
6. Lewis JD, Van de Vyver S, Crisci AJ, Gunther WR, Michaelis VK, Griffin RG, Román-Leshkov Y. A Continuous Flow Strategy for the Coupled Transfer Hydrogenation and Etherification of 5-(Hydroxymethyl)Furfural Using Lewis Acid Zeolites. ChemSusChem. 2014; 7:2255–2265. [PubMed: 25045144]
7. Corma A, Domine ME, Nemeth L, Valencia S. Al-Free Sn-Beta Zeolite as a Catalyst for the Selective Reduction of Carbonyl Compounds (Meerwein–Ponndorf–Verley Reaction). J Am Chem Soc. 2002; 124:3194–3195. [PubMed: 11916388]
8. Corma A, Renz M. A General Method for the Preparation of Ethers Using Water-Resistant Solid Lewis Acids. Angew Chem, Int Ed. 2007; 46:298–300.
9. Jae J, Mahmoud E, Lobo RF, Vlachos DG. Cascade of Liquid-Phase Catalytic Transfer Hydrogenation and Etherification of 5-Hydroxymethylfurfural to Potential Biodiesel Components over Lewis Acid Zeolites. ChemCatChem. 2014; 6:508–513.
10. Hammond C, Conrad S, Hermans I. Simple and Scalable Preparation of Highly Active Lewis Acidic Sn-B. Angew Chem, Int Ed. 2012; 51:11736–11739.
11. Corma A, Nemeth LT, Renz M, Valencia S. Sn-Zeolite Beta as a Heterogeneous Chemoselective Catalyst for Baeyer–Villiger Oxidations. Nature. 2001; 412:423–425. [PubMed: 11473313]
12. Renz M, Blasco T, Corma A, Fornés V, Jensen R, Nemeth L. Selective and Shape-Selective Baeyer–Villiger Oxidations of Aromatic Aldehydes and Cyclic Ketones with Sn-Beta Zeolites and H_2O_2. Chem - Eur J. 2002; 8:4708–4717. [PubMed: 12561111]
13. Moliner M, Román-Leshkov Y, Davis ME. Tin-Containing Zeolites Are Highly Active Catalysts for the Isomerization of Glucose in Water. Proc Natl Acad Sci U S A. 2010; 107:6164–6168. [PubMed: 20308577]
14. Gunther WR, Wang Y, Ji Y, Michaelis VK, Hunt ST, Griffin RG, Román-Leshkov Y. Sn-Beta Zeolites with Borate Salts Catalyse the Epimerization of Carbohydrates Via an Intramolecular Carbon Shift. Nat Commun. 2012; 3:1109. [PubMed: 23047667]
15. Bermejo-Deval R, Orazov M, Gounder R, Hwang SJ, Davis ME. Active Sites in Sn-Beta for Glucose Isomerization to Fructose and Epimerization to Mannose. ACS Catal. 2014; 4:2288–2297.
16. Bermejo-Deval R, et al. Metalloenzyme-Like Catalyzed Isomerizations of Sugars by Lewis Acid Zeolites. Proc Natl Acad Sci U S A. 2012; 109:9727-1–9727-19. [PubMed: 22665778]
17. Choudhary V, Caratzoulas S, Vlachos DG. Insights into the Isomerization of Xylose to Xylulose and Lyxose by a Lewis Acid Catalyst. Carbohydr Res. 2013; 368:89–95. [PubMed: 23353634]
18. Van de Vyver S, Odermatt C, Romero K, Prasomsri T, Roman-Leshkov Y. Solid Lewis Acids Catalyze the Carbon-Carbon Coupling between Carbohydrates and Formaldehyde. ACS Catal. 2015; 5:972–977.
19. Pacheco JJ, Davis ME. Synthesis of Terephthalic Acid Via Diels-Alder Reactions with Ethylene and Oxidized Variants of 5-Hydroxymethylfurfural. Proc Natl Acad Sci U S A. 2014; 111:363–8367.
20. Dusselier M, Van Wouwe P, De Smet S, De Clercq R, Verbelen L, Van Puyvelde P, Du Prez FE, Sels BF. Toward Functional Polyester Building Blocks from Renewable Glycolaldehyde with Sn Cascade Catalysis. ACS Catal. 2013; 3:1786–1800.
21. Wang Y, Lewis JD, Román-Leshkov Y. Synthesis of Itaconic Acid Ester Analogues Via Self-Aldol Condensation of Ethyl Pyruvate Catalyzed by Hafnium Bea Zeolites. ACS Catal. 2016; 6:2739–2744.
22. Van de Vyver S, Román-Leshkov Y. Metalloenzyme-Like Zeolites as Lewis Acid Catalysts for C-C Bond Formation. Angew Chem, Int Ed. 2015; 54:12554–12561.
23. Müller P, Wolf P, Hermans I. Insights into the Complexity of Heterogeneous Liquid-Phase Catalysis: Case Study on the Cyclization of Citronellal. ACS Catal. 2016; 6:2760–2769.
24. Lewis JD, Van de Vyver S, Román-Leshkov Y. Acid–Base Pairs in Lewis Acidic Zeolites Promote Direct Aldol Reactions by Soft Enolization. Angew Chem, Int Ed. 2015; 54:9835–9838.

25. Taarning E, Saravanamurugan S, Spangsberg Holm M, Xiong J, West RM, Christensen CH. Zeolite-Catalyzed Isomerization of Triose Sugars. ChemSusChem. 2009; 2:625–627. [PubMed: 19562790]
26. Holm MS, Saravanamurugan S, Taarning E. Conversion of Sugars to Lactic Acid Derivatives Using Heterogeneous Zeotype Catalysts. Science. 2010; 328:602–605. [PubMed: 20431010]
27. Holm MS, Pagán-Torres YJ, Saravanamurugan S, Riisager A, Dumesic JA, Taarning E. Sn-Beta Catalysed Conversion of Hemicellulosic Sugars. Green Chem. 2012; 14:702–706.
28. De Clercq R, Dusselier M, Christiaens C, Dijkmans J, Iacobescu RI, Pontikes Y, Sels BF. Confinement Effects in Lewis Acid-Catalyzed Sugar Conversion: Steering toward Functional Polyester Building Blocks. ACS Catal. 2015; 5:5803–5811.
29. Luo HY, Lewis JD, Román-Leshkov Y. Lewis Acid Zeolites for Biomass Conversion: Perspectives and Challenges on Reactivity, Synthesis, and Stability. Annu Rev Chem Biomol Eng. 2016; 7:663–692. [PubMed: 27146555]
30. Bermejo-Deval R, Gounder R, Davis ME. Framework and Extraframework Tin Sites in Zeolite Beta React Glucose Differently. ACS Catal. 2012; 2:2705–2713.
31. Wolf P, et al. Nmr Signatures of the Active Sites in Sn-B Zeolite. Angew Chem, Int Ed. 2014; 53:10179–10183.
32. Dijkmans J, Gabriels D, Dusselier M, de Clippel F, Vanelderen P, Houthoofd K, Malfliet A, Pontikes Y, Sels BF. Productive Sugar Isomerization with Highly Active Sn in Dealuminated B Zeolites. Green Chem. 2013; 15:2777–2785.
33. Tang B, Dai W, Wu G, Guan N, Li L, Hunger M. Improved Postsynthesis Strategy to Sn-Beta Zeolites as Lewis Acid Catalysts for the Ring-Opening Hydration of Epoxides. ACS Catal. 2014; 4:2801–2810.
34. Bare SR, Kelly SD, Sinkler W, Low JJ, Modica FS, Valencia S, Corma A, Nemeth LT. Uniform Catalytic Site in Sn-B-Zeolite Determined Using X-Ray Absorption Fine Structure. J Am Chem Soc. 2005; 127:12924–12932. [PubMed: 16159286]
35. Gunther WR, Michaelis VK, Caporini MA, Griffin RG, Roman-Leshkov Y. Dynamic Nuclear Polarization Nmr Enables the Analysis of Sn-Beta Zeolite Prepared with Natural Abundance 119sn Precursors. J Am Chem Soc. 2014; 136:6219–6222. [PubMed: 24697321]
36. Kolyagin YG, Yakimov AV, Tolborg S, Vennestrøm PN, Ivanova II. Application of 119sn Cpmg Mas Nmr for Fast Characterization of Sn Sites in Zeolites with Natural 119sn Isotope Abundance. J Phys Chem Lett. 2016; 7:1249–1253. [PubMed: 26978430]
37. Harris RK, Becker ED. Nmr Nomenclature: Nuclear Spin Properties and Conventions for Chemical Shifts - Iupac Recommendations. J Magn Reson. 2002; 156:323–326.
38. Emeis CA. Determination of Integrated Molar Extinction Coefficients for Infrared Absorption Bands of Pyridine Adsorbed on Solid Acid Catalysts. J Catal. 1993; 141:347–54.
39. de la Torre O, Renz M, Corma A. Biomass to Chemicals: Rearrangement of B-Pinene Epoxide into Myrtanal with Well-Defined Single-Site Substituted Molecular Sieves as Reusable Solid Lewis-Acid Catalysts. Appl Catal, A. 2010; 380:165–171.
40. Heitmann GP, Dahlhoff G, Hölderich WF. Modified Beta Zeolites as Catalysts for the Beckmann Rearrangement of Cyclohexanone Oxime. Appl Catal, A. 1999; 185:99–108.
41. Corma A, Llabrés i, Xamena FX, Prestipino C, Renz M, Valencia S. Water Resistant, Catalytically Active Nb and Ta Isolated Lewis Acid Sites, Homogeneously Distributed by Direct Synthesis in a Beta Zeolite. J Phys Chem C. 2009; 113:11306–11315.
42. Corma A, Domine ME, Valencia S. Water-Resistant Solid Lewis Acid Catalysts: Meerwein-Ponndorf-Verley and Oppenauer Reactions Catalyzed by Tin-Beta Zeolite. J Catal. 2003; 215:294–304.
43. Roy S, Bakhmutsky K, Mahmoud E, Lobo RF, Gorte RJ. Probing Lewis Acid Sites in Sn-Beta Zeolite. ACS Catal. 2013; 3:573–580.
44. Harris JW, Cordon MJ, Di Iorio JR, Vega-Vila JC, Ribeiro FH, Gounder R. Titration and Quantification of Open and Closed Lewis Acid Sites in Sn-Beta Zeolites That Catalyze Glucose Isomerization. J Catal. 2016; 335:141–154.
45. Laurence C, Graton J, Gal JF. An Overview of Lewis Basicity and Affinity Scales. J Chem Educ. 2011; 88:1651–1657.

46. Laurence, C., Gal, JF. Lewis Basicity and Affinity Scales: Data and Measurement. John Wiley & Sons; Hoboken, N.J: 2009.
47. Li G, Pidko EA, Hensen EJM. Synergy between Lewis Acid Sites and Hydroxyl Groups for the Isomerization of Glucose to Fructose over Sn-Containing Zeolites: A Theoretical Perspective. Catal Sci Technol. 2014; 4:2241–2250.
48. Yang G, Pidko EA, Hensen EJM. The Mechanism of Glucose Isomerization to Fructose over Sn-Bea Zeolite: A Periodic Density Functional Theory Study. ChemSusChem. 2013; 6:1688–1696. [PubMed: 23943294]
49. Brunner E, Pfeifer H. Nmr Spectroscopic Techniques for Determining Acidity and Basicity. Mol Sieves. 2007; 6:1–43.
50. Ripmeester JA. Surface Acid Site Characterization by Means of Cp/Mas Nitrogen-15 Nmr. J Am Chem Soc. 1983; 105:2925–7.
51. Michel D, Germanus A, Pfeifer H. Nitrogen-15 Nuclear Magnetic Resonance Spectroscopy of Adsorbed Molecules. J Chem Soc, Faraday Trans. 1982; 178:237–54.
52. Lezcano-Gonzalez I, Vidal-Moya A, Boronat M, Blasco T, Corma A. Modelling Active Sites for the Beckmann Rearrangement Reaction in Boron-Containing Zeolites and Their Interaction with Probe Molecules. Phys Chem Chem Phys. 2010; 12:6396–6403. [PubMed: 20454729]
53. Freude D, Pfeifer H, Schmidt A, Standte B. Characterization of Acid Centers in Hy Zeolite by Nmr Studies of the Interaction of Hydroxyl Groups with Pyridine. Z Phys Chem. 1984; 265:250–256.
54. Corma A, Nemeth LT, Renz M, Valencia S. Sn-Zeolite Beta as a Heterogeneous Chemoselective Catalyst for Baeyer-Villiger Oxidations. Nature. 2001; 412:423–425. [PubMed: 11473313]
55. Gunther WR, Duong Q, Roman-Leshkov Y. Catalytic Consequences of Borate Complexation and Ph on the Epimerization of L-Arabinose to L-Ribose in Water Catalyzed by Sn-Beta Zeolite with Borate Salts. J Mol Catal A: Chem. 2013; 379:294–302.
56. Mal NK, Ramaswamy V, Rajamohanan PR, Ramaswamy AV. Sn-Mfi Molecular Sieves: Synthesis Methods, 29Si Liquid and Solid Mas-Nmr, 119sn Static and Mas Nmr Studies. Microporous Mater. 1997; 12:331–340.
57. Gaydhankar TR, Joshi PN, Kalita P, Kumar R. Optimal Synthesis Parameters and Application of Sn-Mcm-41 as an Efficient Heterogeneous Catalyst in Solvent-Free Mukaiyama-Type Aldol Condensation. J Mol Catal A: Chem. 2007; 265:306–315.
58. Pines A, Gibby MG, Waugh JS. Proton-Enhanced Nmr of Dilute Spins in Solids. J Chem Phys. 1973; 59:569–590.
59. Pines A, Gibby MG, Waugh JS. Proton-Enhanced Nuclear Induction Spectroscopy. Method for High-Resolution Nmr of Dilute Spins in Solids. J Chem Phys. 1972; 56:1776–1777.
60. Bennett AE, Rienstra CM, Auger M, Lakshmi KV, Griffin RG. Heteronuclear Decoupling in Rotating Solids. J Chem Phys. 1995; 103:6951–8.
61. Gibby M, Griffin R, Pines A, Waugh J. High Resolution Nmr of 15 N in Solids. Chem Phys Lett. 1972; 17:80–81.
62. Frisch, MJ., et al. Gaussian 09. Gaussian, Inc; Wallingford, CT: 2009.
63. Weigend F, Ahlrichs R. Balanced Basis Sets of Split Valence, Triple Zeta Valence and Quadruple Zeta Valence Quality for H to Rn: Design and Assessment of Accuracy. Phys Chem Chem Phys. 2005; 7:3297–3305. [PubMed: 16240044]
64. Andrae D, Haeussermann U, Dolg M, Stoll H, Preuss H. Energy-Adjusted Ab Initio Pseudopotentials for the Second and Third Row Transition Elements. Theor Chim Acta. 1990; 77:123–41.
65. Metz B, Stoll H, Dolg M. Small-Core Multiconfiguration-Dirac-Hartree-Fock-Adjusted Pseudopotentials for Post-D Main Group Elements: Application to Pbh and Pbo. J Chem Phys. 2000; 113:2563–2569.
66. Schweitzer D, Spiess HW. Nitrogen-15 Nmr of Pyridine in High Magnetic: Fields. J Magn Reson. 1974; 15:529–539.
67. Solum MS, Altmann KL, Strohmeier M, Berges DA, Zhang Y, Facelli JC, Pugmire RJ, Grant DM. 15n Chemical Shift Principal Values in Nitrogen Heterocycles. J Am Chem Soc. 1997; 119:9804–9809.

68. Hemmann F, Agirrezabal-Telleria I, Kemnitz E, Jäger C. Probing Slow Chemical Exchange of Pyridine Molecules at Acid Magnesium Hydroxide Fluoride Surfaces by 15n Nmr. J Phys Chem C. 2013; 117:14710–14716.
69. Lorente P, Shenderovich IG, Golubev NS, Denisov GS, Buntkowsky G, Limbach HH. 1h/15n Nmr Chemical Shielding, Dipolar 15n, 2h Coupling and Hydrogen Bond Geometry Correlations in a Novel Series of Hydrogen-Bonded Acid–Base Complexes of Collidine with Carboxylic Acids. Magn Reson Chem. 2001; 39:S18–S29.
70. Shenderovich IG, Buntkowsky G, Schreiber A, Gedat E, Sharif S, Albrecht J, Golubev NS, Findenegg GH, Limbach HH. Pyridine-15 Na Mobile Nmr Sensor for Surface Acidity and Surface Defects of Mesoporous Silica. J Phys Chem B. 2003; 107:1924–11939.
71. Schurko RW, Wasylishen RE. Nitrogen-15 Nmr Study of Solid Cobaloximes Containing 15n-Labeled Pyridine and Aniline. J Phys Chem A. 2000; 104:3410–3420.
72. Gurinov AA, Rozhkova YA, Zukal At, Čejka Ji, Shenderovich IG. Mutable Lewis and Brønsted Acidity of Aluminated Sba-15 as Revealed by Nmr of Adsorbed Pyridine-15N. Langmuir. 2011; 27:12115–12123. [PubMed: 21859107]
73. Ramsey NF. Electron Coupled Interactions between Nuclear Spins in Molecules. Phys Rev. 1953; 91:303–7.
74. van der Waal JC, Tan K, van Bekkum H. Zeolite Titanium Beta: A Selective and Water Resistant Catalyst in Meerwein-Ponndorf-Verley-Oppenauer Reactions. Catal Lett. 1996; 41:63–67.
75. Li YP, Head-Gordon M, Bell AT. Analysis of the Reaction Mechanism and Catalytic Activity of Metal-Substituted Beta Zeolite for the Isomerization of Glucose to Fructose. ACS Catal. 2014; 4:1537–1545.
76. Boronat M, Corma A, Renz M, Viruela PM. Predicting the Activity of Single Isolated Lewis Acid Sites in Solid Catalysts. Chem -Eur J. 2006; 12:7067–7077. [PubMed: 16933346]
77. Fenzke D, Hunger M, Pfeifer H. Determination of Nuclear Distances and Chemical-Shift Anisotropy from Proton Mas Nmr Sideband Patterns of Surface Hydroxyl Groups. J Magn Reson. 1991; 95:477–83.
78. Pearson RG. Absolute Electronegativity and Hardness: Application to Inorganic Chemistry. Inorg Chem. 1988; 27:734–40.
79. Corma A, Garcia H. Lewis Acids: From Conventional Homogeneous to Green Homogeneous and Heterogeneous Catalysis. Chem Rev. 2003; 103:4307–4365. [PubMed: 14611265]
80. Zhan CG, Nichols JA, Dixon DA. Ionization Potential, Electron Affinity, Electronegativity, Hardness, and Electron Excitation Energy: Molecular Properties from Density Functional Theory Orbital Energies. J Phys Chem A. 2003; 107:4184–4195.
81. Shetty S, Pal S, Kanhere DG, Goursot A. Structural, Electronic, and Bonding Properties of Zeolite Sn-Beta: A Periodic Density Functional Theory Study. Chem - Eur J. 2006; 12:518–523.
82. Marschner C. Hafnium: Stepping into the Limelight! Angew Chem, Int Ed. 2007; 46:6770–6771.
83. Blasco T, Camblor MA, Corma A, Esteve P, Guil JM, Martinez A, Perdigon-Melon JA, Valencia S. Direct Synthesis and Characterization of Hydrophobic Aluminum-Free Ti-Beta Zeolite. J Phys Chem B. 1998; 102:75–88.
84. Dijkmans J, Dusselier M, Gabriëls D, Houthoofd K, Magusin PCMM, Huang S, Pontikes Y, Trekels M, Vantomme A, Giebeler L, et al. Cooperative Catalysis for Multistep Biomass Conversion with Sn/Al Beta Zeolite. ACS Catal. 2015; 5:928–940.
85. Hammond C, Conrad S, Hermans I. Simple and Scalable Preparation of Highly Active Lewis Acidic Sn-B. Angew Chem, Int Ed. 2012; 51:11736–11739.
86. Dijkmans J, Demol J, Houthoofd K, Huang S, Pontikes Y, Sels B. Post-Synthesis Snβ: An Exploration of Synthesis Parameters and Catalysis. J Catal. 2015; 330:545–557.
87. Wolf P, Hammond C, Conrad S, Hermans I. Post-Synthetic Preparation of Sn-, Ti-and Zr-Beta: A Facile Route to Water Tolerant, Highly Active Lewis Acidic Zeolites. Dalton Trans. 2014; 43:4514–4519. [PubMed: 24407516]
88. van der Graaff WN, Li G, Mezari B, Pidko EA, Hensen EJ. Synthesis of Sn-Beta with Exclusive and High Framework Sn Content. ChemCatChem. 2015; 7:1152–1160.

89. Luo HY, Consoli DF, Gunther WR, Román-Leshkov Y. Investigation of the Reaction Kinetics of Isolated Lewis Acid Sites in Beta Zeolites for the Meerwein–Ponndorf–Verley Reduction of Methyl Levulinate to γ-Valerolactone. J Catal. 2014; 320:198–207.

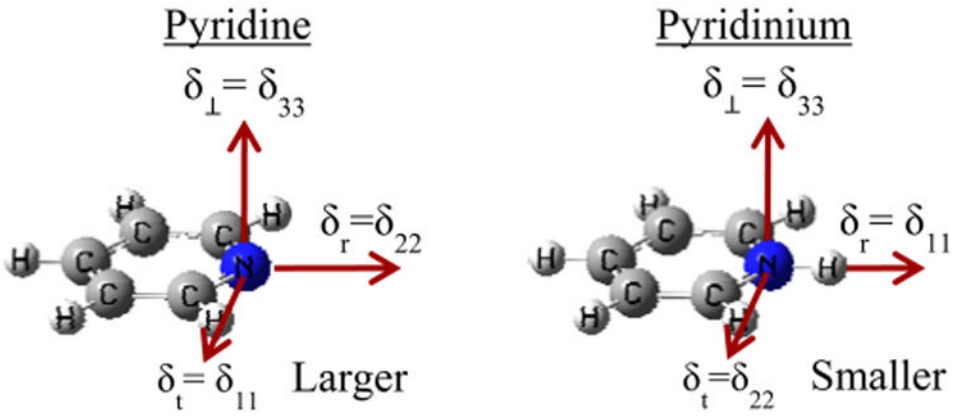

Figure 1.

Rotation of CSA components into the pyridine radial δ_r, tangential δ_v, and perpendicular $\delta_\perp$ reference frame. The pyridine δ_t decreases upon binding to a proton or Lewis acid site, causing it to change from δ_{11} to δ_{22} in NMR nomenclature ($\delta_{33} \leq \delta_{22} \leq \delta_{11}$).

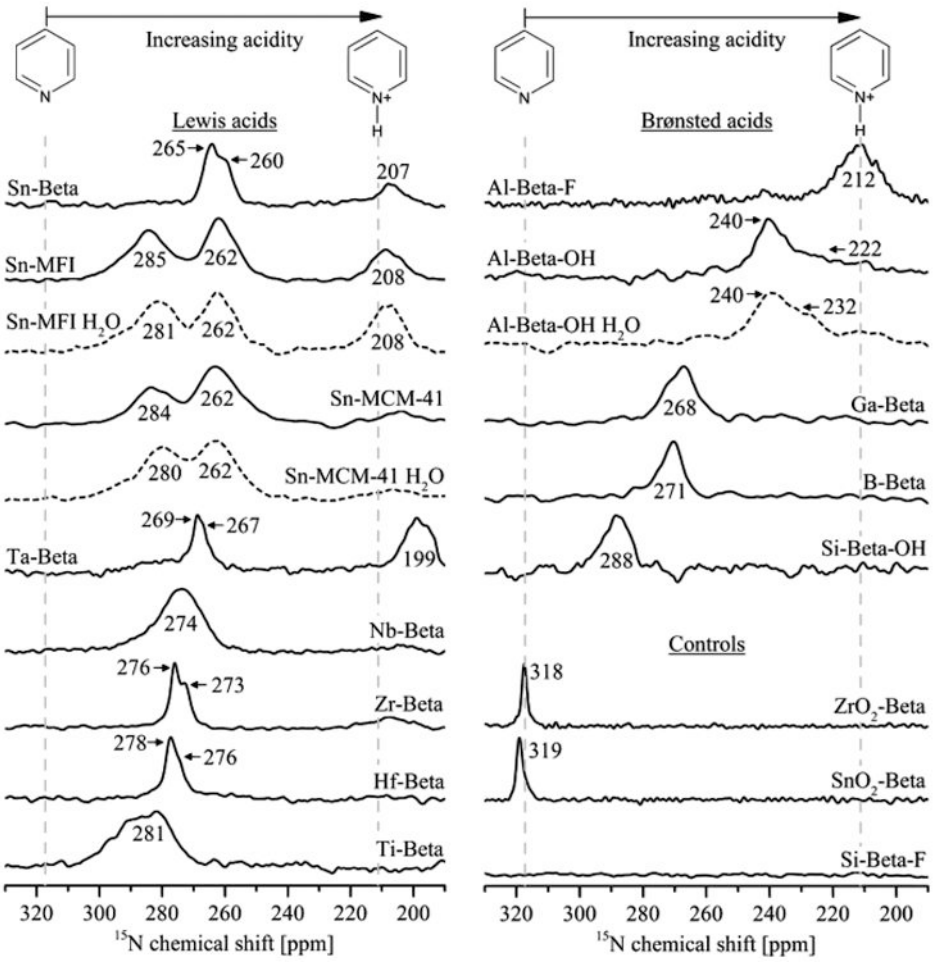

Figure 2.

^{15}N CP MAS NMR of pyridine adsorbed on metal-substituted zeolites. Spinning sidebands appear outside the field of view. Colored dashed data correspond to spectra of hydrated samples. While vertical gray lines correspond to nonbound pyridine (left) and pyridinium (right). H–Al–Beta–F had a Si/Al = 50, H–Al–Beta–OH had a Si/Al = 19, and all other materials had Si/metal ≈100.

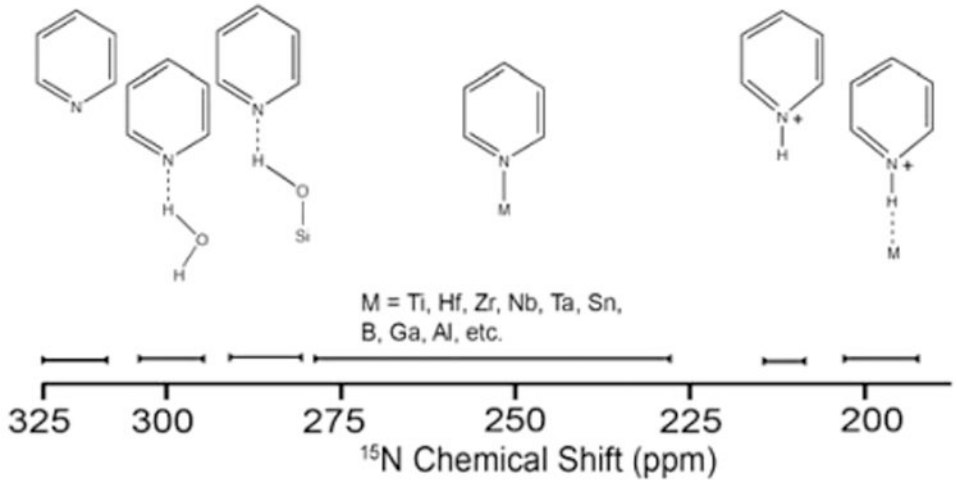

Figure 3.
^{15}N solid-state NMR chemical shift scale of various pyridine binding environments.

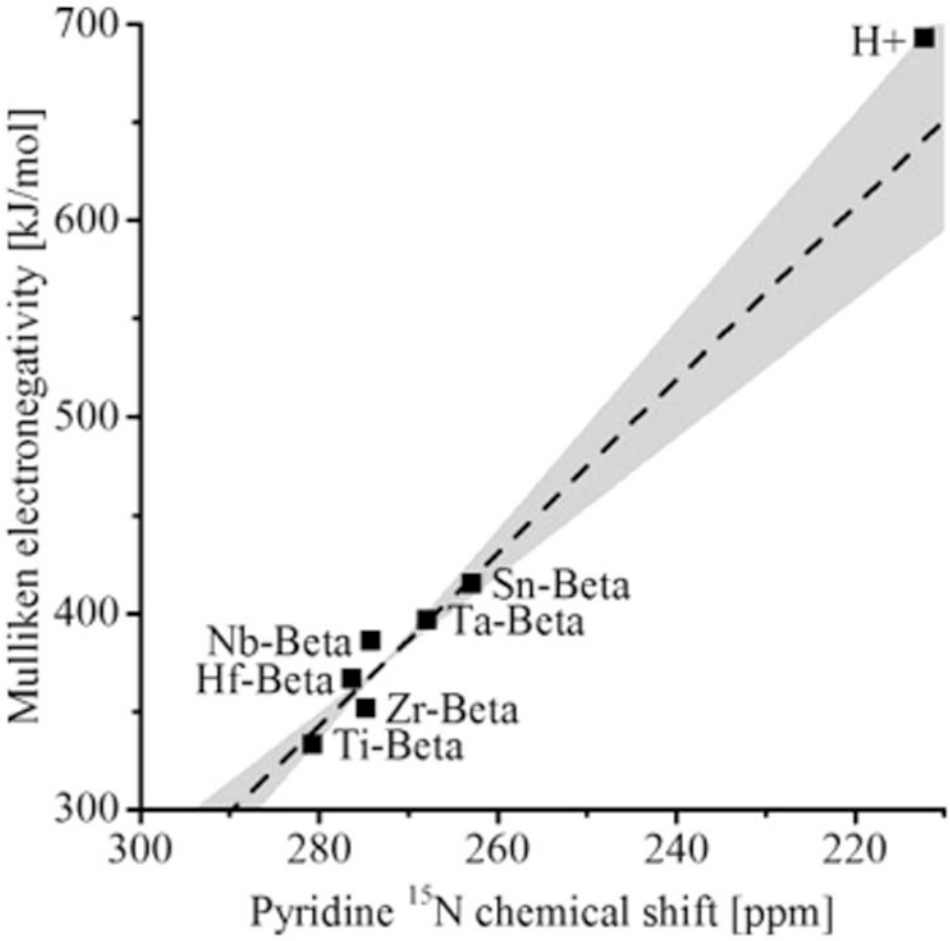

Figure 4.

Experimental Mulliken electronegativity vs pyridine ^{15}N MAS NMR chemical shift. The chemical shift shown is unweighted average of the isotropic chemical shifts associated with strong and weak sites. The dashed line and gray envelope show a regression with standard errors.

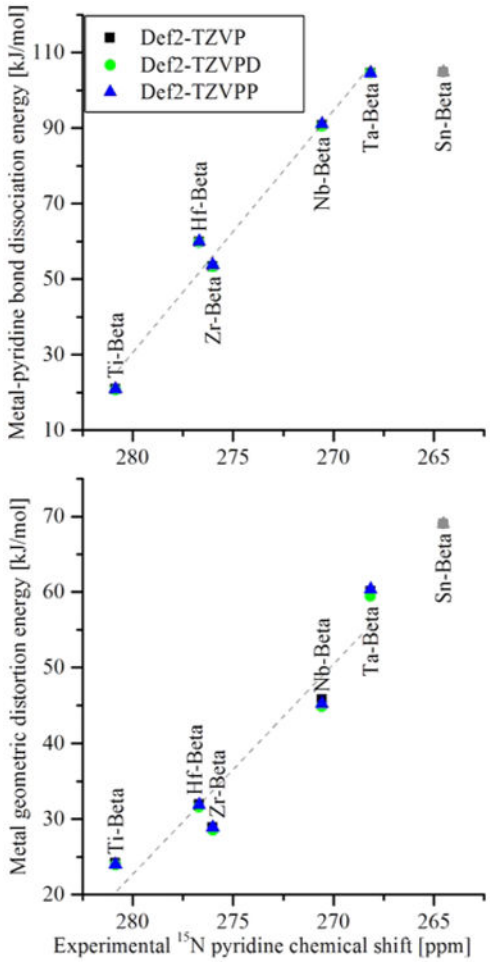

Figure 5.

Distortion and dissociation energetics associated with pyridine adsorption calculated with DFT. The chemical shift shown is unweighted average of the isotropic chemical shifts associated with strong and weak sites.

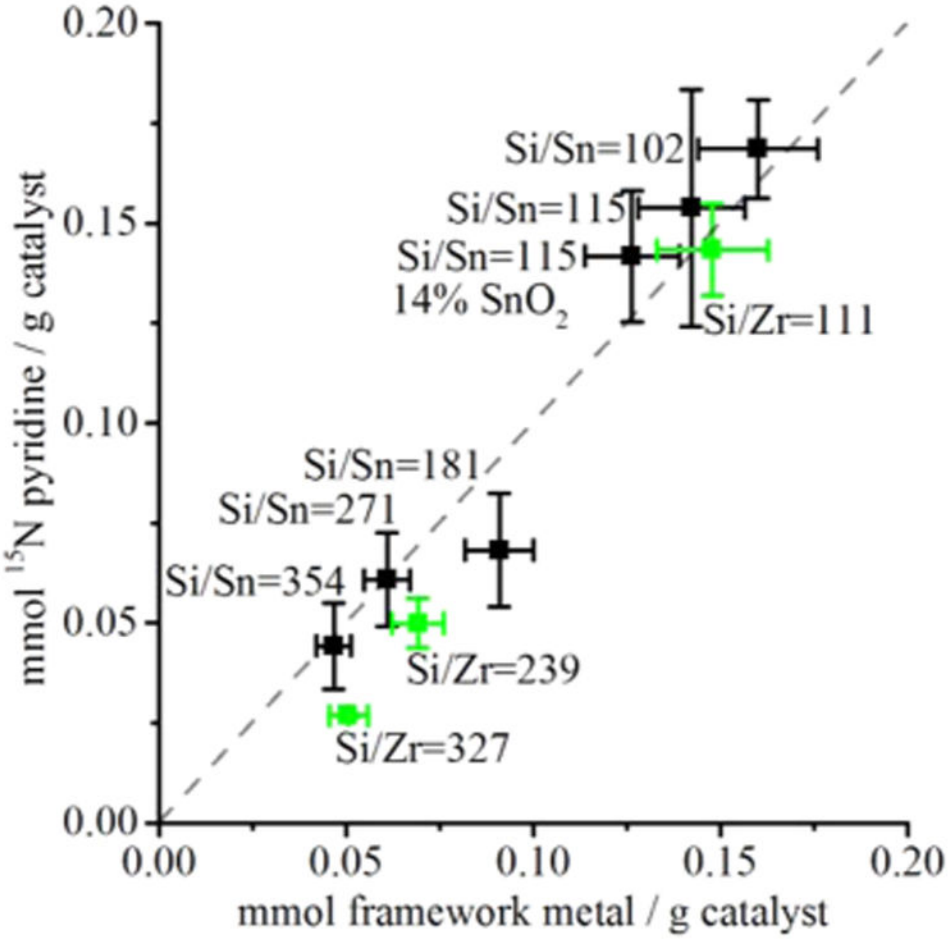

Figure 6.

Quantification of adsorbed pyridine using ^{15}N MAS NMR. The dotted line represents a parity line. The Y-error bars are based on the signal-to-noise of each spectra; each experimental data point was analyzed in triplicate, and the error bars represent two times the sample standard deviation. X-error bars represent the range of errors (ca. 10%) typically obtained during elemental analysis, including zeolite dissolution and ICP characterization.

Table 1

Summary of ^{15}N Solid-State NMR Chemical Shift of Nitrogen Heterocycles in Various Environments[a]

sample	δ_{iso} (ppm, ± 1)	Ω (ppm)	κ	δ_t (ppm)	δ_r (ppm)	$\delta_\perp$ (ppm)	ref
pyridine	317	622	0.46	580	413	−42	66,67
physisorbed pyridine (Mg–F–OH)	330	n.d.	n.d.	n.d.	n.d.	n.d.	68
physisorbed pyridine Beta zeolite	319	n.d.	n.d.	n.d.	n.d.	n.d.	this study
collidine	307	539	0.4	530	375	9	69
H_2O-pyridine	300	n.d.	n.d.	n.d.	n.d.	n.d.	70
Si–O–H-pyridine	290	n.d.	n.d.	n.d.	n.d.	n.d.	70
Mg–O–H-pyridine	292	n.d.	n.d.	n.d.	n.d.	n.d.	68
SnBeta-pyridine	264	390 ± 20	0.9 ± 0.1	380	401	11	this study
ZrBeta-pyridine	278	365 ± 20	0.8 ± 0.1	375	411	47	this study
MBeta-pyridine (range)	270 ± 10	370 ± 20	0.80 ± 0.1	–	–	–	this study
Co-pyridine	265	488	0.96	423	430	−58	71
Mg-pyridine	280	n.d.	n.d.	n.d.	n.d.	n.d.	68
Al-pyridine	233	n.d.	n.d.	n.d.	n.d.	n.d.	72
pyridinium	211	352	0.62	284	351	−1	67
Mg-pyridinium	205	n.d.	n.d.	n.d.	n.d.	n.d.	68
collidine-$HB(Ph)_4$	187	250	0.05	189	309	59	69

[a]NB: All ^{15}N data is referenced relative to liquid ammonia (0 ppm). Solid $^{15}NH_4Cl$ is 39.3 ppm (relative to liquid ammonia), solid $^{15}NH_4NO_3$ is 22 ppm (relative to liquid ammonia), and $CH_3{}^{15}NO_2$ (neat) is 380.55 ppm (relative to liquid ammonia).[5]

Table 2

Experimental Values for Ionization Potential (I), Electron Affinity (A), Mulliken Electronegativity, and Hardness Taken from Literature.[78]

	ionization potential, I (kJ/mol)	**electron affinity, A (kJ/mol)**	**mulliken electronegativity, χ (kJ/mol)**	**hardness, η (kJ/mol)**
pyridine	900	−60	420	500
Ti	658	8	333	325
Hf	650	80	370	300
Zr	660	41	351	310
Nb	670	100	400	300
Ta	761	31	397	366
Sn	708	121	410	294
B	800	27	414	387
Ga	600	30	310	280
Al	578	44	312	267
Si	786	134	460	326
H+	1310	72	693	620
proportional to	HOMO	LUMO	HOMO+LUMO	HOMO-LUMO

Table 3

Calculated Pyridine-Metal (M–N) Bond Distances, Metal–Oxygen (M–O, M=O) Bond Distances, Bond Dissociation (D_0), and Relaxation ($\Delta E_{M\ relax}$) Energies for Several Lewis Acid Zeolites[a]

material	M–N (Å)	M–O (Å)	M=O (Å)	D_0 (kJ/mol)	Δ*E*M relax (kJ/mol)
Ti-Beta	2.67	1.79	n.a.	21	24
Hf-Beta	2.58	1.94	n.a.	60	32
Zr-Beta	2.61	1.94	n.a.	53	29
Nb-Beta	2.44	1.91	1.73	91	45
Ta-Beta	2.41	1.92	1.76	105	59
Sn-Beta[b]	2.39	1.93	n.a.	105	69

[a] +DFT methods used: B3LYP/Def2-TZVPD.

[b] Denotes an extended model.

J Phys Chem C Nanomater Interfaces. Author manuscript; available in PMC 2017 May 05.